An Efficient *LCL-T*-Based Compact Resonant Converter for On-Board Charger

Akash Deo, *Student Member, IEEE*, and Arun Kumar Verma, *Senior Member, IEEE*

***Abstract*—Numerous efforts are underway to minimize the dimensions of electric vehicle on-board chargers. This can be attained by enhancing the power density without sacrificing the converter efficiency. Magnetic integration is one of the widely used techniques to achieve a higher power density. For on-board chargers, *LLC*-based resonant converters are a common option where optimization of switching frequency, power density, and efficiency has been accomplished in a number of studies. Efficiency and power density are still required to satisfy the demands of electric car charging, notwithstanding the trade-off between soft-switching over the load range. *LCL-T*-based resonant converters offers a promising solution to this problem, which are yet to be explored with magnetic integration. This article proposes a *LCL-T*-based resonant converter with magnetic integration to achieve higher power density. Above all, this magnetic integration has been achieved using simple switching scheme with fixed frequency operation. The converter maintains zero voltage switching in all the switches and zero current switching in both the diodes over the entire load range. The proposed magnetic integration has been validated by finite element analysis (FEA) in Ansys maxwell simulation software. A 2 KW prototype with 400 V input and 200–400 V output has been tested in the lab. The converter achieves highest efficiency of 98.15% and integrated transformer maintains a power density of 25.57 W/cm^3.**

***Index Terms*—Magnetic integration, on-board charger (OBC), resonant immittance converter (RIC), soft switching, zero voltage switching (ZVS).**

I. INTRODUCTION

PLUG-IN electric vehicles (PEV) are becoming more popular due to their energy efficiency and environment friendliness [1]. Batteries are major components of electric vehicle and their charging mechanism plays an important role in achieving healthy charging of battery stacks. PEVs generally consist of an on-board charger, which is amalgamation of two stages. The first stage is a front-end PFC circuit that generates an output, which is free from input current harmonics and exhibits high power factor [2]. The second stage is a dc–dc converter, which provides galvanic isolation in the charger. Several isolated dc–dc converters have been investigated and can be separated into the different categories to attain a high conversion efficiency and necessary charging profiles. Resonant-based dc–dc converters consists of three or more resonant elements in different arrangements which can result in various immittance converter topologies [3]. Apart from immittance converter topologies, the *LLC* resonant converters among other dc/dc converters has always been a popular choice due to its exceptional soft switching performance, low voltage stress on switching devices, and friendly magnetic integration. *LLC* resonant converters are still developing even though they are widely used in many different industry applications. The demands of various applications continue to call for a number of tradeoffs between efficiency, size/volume of magnetic cores, switching frequency, and voltage regulation capability. This has led to the continuous development of new topological variants, modulation techniques, magnetic integration, and design approaches. Wouters and Martinez [4] presented the potential of inductor-integrated transformers with state of art designs, such as PCB windings, matrix transformers, different winding arrangements and core shape customization. The goal of attaining higher efficiency and power density is a prevalent paradigm for dc–dc power converters. In order to increase the power density, magnetic integration has been the most suitable option to maintain the power level by reducing number of magnetic elements. The *LLC* converter in [5] proposes transformer and inductor on the same EE core using decoupled integration approach. The converter reports higher power density but efficiency remains low at light load. In [6], resonant inductor of an *LLC* resonant converter is placed on the transformer's secondary side to create the *CLL* resonant converter. The converter uses two ER core planar structure for magnetic integration. However, converter achieves higher power density with increased core losses resulting in low peak efficiency. An integrated planar magnetic structure on a EE core is proposed in [7] in this work. The same winding can act as inductor or transformer alternatively in the switching periods. Hence, high efficiency and high power density can be achieved for *LLC* resonant converter. However, the converter suffers from power rating constraint as the same winding needs to sustain transformer and resonant inductor function. The converter in [8] optimizes leakage inductance using horizontal gap on EI core but the peak efficiency remains 96.5% in 200 W prototype.

Apart from *LLC* resonant converter, magnetic integration has also been reported in some hybrid topologies. A *CLLLC* converter in [9] uses magnetic shunts to control leakage in planar structure. The converter achieves decoupling between

Received 10 March 2025; revised 4 July 2025, 8 September 2025, and 31 October 2025; accepted 8 December 2025. Date of publication 11 December 2025; date of current version 25 February 2026. This work was supported by the SERB, India's financial assistance under Grant SERB/CRG/2022/005797. Recommended for publication by Associate Editor M. Wang. *(Corresponding author: Akash Deo.)*

The authors are with the Department of Electrical Engineering, Indian Institute of Technology, Jammu 181221, India (e-mail: 2023REE1028@iitjammu.ac.in; arun.verma@iitjammu.ac.in).

Color versions of one or more figures in this article are available at https://doi.org/10.1109/TPEL.2025.3643182.

Digital Object Identifier 10.1109/TPEL.2025.3643182

the magnetizing inductance and primary and secondary leakage inductance. However, space occupied by the magnetic shunts diminishes power density of the converter. Li et al. [10] presented a modified core designed for low voltage high current application. Two transformers and four output inductors have been assembled on the modified core structure to enhance the power density of the converter. Wu et al. [11] proposed a hybrid resonant converter integrating autotransformer and two transformers into one core. The converter is designed for low voltage high current applications, such as data center. The converter reduces footprint, volume and core loss in comparison to discrete transformer structures by using a merged core. A dual transformer-based dual active bridge (DAB) converter in [12] uses a split UI core for magnetic integration in planar structure. Split UI core integration can reduce number of printed circuit board (PCB) layers in planar structure and control leakage inductance. A high frequency low power integrated magnetic structure with high efficiency and high power density is shown in [13]. The converter attains soft switching independent of load changes and eliminates the need of additional *LC* branch. A current fed DAB is proposed in [14] integrates two input dc inductors, a series and a transformer on the same core. However, the converter uses customized core but achieves high power density by diminishing volume. In [15], a current fed DAB integrates two dc inductors, transformer and uses leakage inductance to eliminate the additional external inductor using a single EE42 core. The converter uses distributed primary side windings as coupled dc inductors and distributed secondary side windings.

In order to increase the power density, PCB-based planar designs have been popular choice. Nonetheless, inadequate conductivity in dielectric materials and parasitic capacitance may result in suboptimal thermal performance, while reduced isolation thickness might exacerbate parasitic capacitance [16]. Custom cores and ferrite shaping are also widely accepted options for integrated magnetics designs but configuration of cooling methods and vias may result in elevated expenses for customized cores [17], whereas ferrite shaping is limited by material properties and manufacturing in case of custom cores [4].

LCL-T resonant topology-based converters have not been explored with magnetic integration. Although *LCL-T*-based resonant converters have been reported in several works exploiting its immittance characteristics in order to achieve desirable charging profiles. The converter presented in [18] exhibits inherent constant current (CC) charging profile due to *LCL-T* RIC on the primary side but fails to maintain the efficiency in constant voltage (CV) charging mode due to high circulating currents in diodes. Wang et al. [19] kept *LCCL* immittance network on the secondary side of the transformer to mitigate the problem of circulating currents in CV mode. The converter achieves desirable profiles without any control complexity and sensing but design uses two diode full bridges on the secondary side resulting in low component utilization. This problem of under component utilization has been addressed in [20] using *LCL-T* resonant network on the secondary side and two diode half bridges connected in parallel. The converter achieves CC mode to CV mode transformation exploiting RIC properties of *LCL-T* without any control loop and fixed frequency operation. However, the presence of multiple magnetic components diminishes the power density and occupies more space on the board making overall system bulkier. A *CLCLC* type immittance resonant DAB with dual unbalanced modulation strategy is presented in [21]. The converter achieves bidirectional operation with high efficiency but power density remains low with high control complexity.

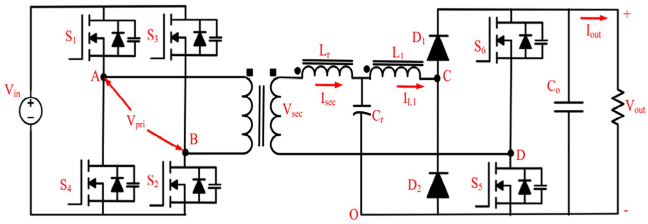

Fig. 1. Proposed DC–DC converter with integrated magnetics.

In order to derive a high power density, high efficiency and cost effective design, this article proposes a *LCL-T* RIC-based resonant converter with integrated magnetics. Transformer and two inductors of the *LCL-T* network have been integrated on single EE core. Some of the key features of the proposed converter are as follows.

1) The proposed converter exhibits higher power density maintaining high efficiency than the converters presented in [18], [19], [20], and [21]. Also, absence of two inductors makes the system less bulky and more compact.
2) The proposed converter attains soft switching operation in all the switches on the primary side and secondary side of the transformer, it also exhibits zero current switching in the diodes on the secondary sides over the entire load range.
3) The proposed resonant converter exhibits automatic charging mode transition. This is achieved by the converter without any sensing and control.
4) The converter achieves high power density without any customized core and specific ferrite shaping. The proposed converter uses EE6527 core with CF297 material.

The rest of this article is organized as follows. Section II discusses circuit configuration and operating modes of the proposed converter. Section III discusses transformer-inductor integration physical structure, coupled *LCL-T* resonant network characteristics and electrical circuit analysis of the equivalent electrical circuit with integrated magnetics. Section IV presents a comparison of discrete magnetic structures against integrated magnetic structure using finite element analysis (FEA) and prototype demonstration and hardware validation of the proposed converter. Finally, Section V concludes this article.

II. PROPOSED CONVERTER WITH INTEGRATED MAGNETICS TRANSFORMER

A. *Circuit Configuration*

The proposed *LCL-T*-based resonant converter with integrated magnetics is depicted in Fig. 1. On the primary side of the transformer, the converter features a full bridge high-frequency inverter; on the secondary side, there are two switches and two diodes. Two diodes and two switches are connected as two half bridges connected in parallel across the load. The transformer is

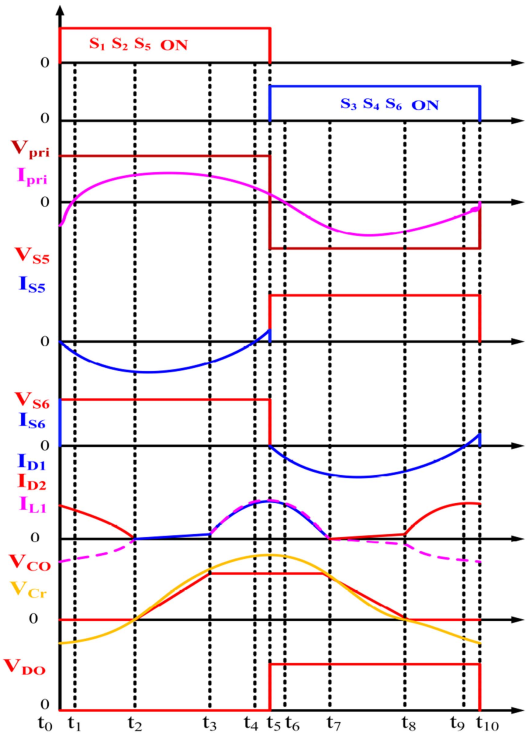

Fig. 2. Typical waveforms of the proposed resonant converter over one switching cycle.

wound on the middle leg of the EE core, and the two inductors are wound on the side columns of the EE core. The two inductors L_r and L_1 of *LCL-T* network are wound as coupled inductors on the same core as indicated in Fig. 1. V_{in} is input voltage of the converter. V_{pri}, I_{pri}, V_{sec}, and I_{sec} indicates primary voltage, primary current, secondary voltage, and secondary current, respectively. The windings L_r and L_1 represents resonant inductor and second inductor windings of the *LCL-T* network and C_r is resonant capacitor. The battery is modeled as equivalent load resistance R_L. Resonant frequency and switching frequency have been kept same for the *LCL* network. Typical waveforms of the proposed converter over a switching cycle are shown in Fig. 2. The details of the circuit operating modes are discussed in detail in Section II-B.

B. Operating Modes

The operating modes of the proposed converter shown in Fig. 3 are as follows.

Mode 1 (t_0-t_1): Body diodes of switch S_1 and S_2 are conducting, leading to zero voltage turn-ON of S_1 and S_2. The primary current I_{pri} is negative and decaying to zero. The load capacitor C_o supplies power to the load. The inductor L_r-C_r resonates through the body diode of the switch, S_5 and the inductor L_1-C_r resonates through the diode D_2.

Mode 2 (t_1-t_2): The primary current crosses zero at a time instant t_1 and becomes positive. Switches S_1 and S_2 turns ON at zero voltage. The voltage across the resonant capacitor V_{C_r} is zero at time instant t_2, thus turning OFF the diode D_2. The load capacitor C_o continues to supply power to the load

$$\begin{cases} V_{C_r}(t-t_1) = \frac{V_{\text{in}}}{n} - \left[\frac{V_{\text{in}}}{n} - V_{C_r}(t_1)\right] \cos\omega_0(t-t_1) \\ +Z_0 I_{L_r}(t_1)\sin\omega_0(t-t_1) \\ I_{L_r}(t-t_1) = I_{L_r}(t_1)\cos\omega_0(t-t_1) + \frac{\frac{V_{\text{in}}}{n} - V_{C_r}(t_1)}{Z_0} \\ \sin\omega_0(t-t_1) \\ V_{C_r}(t-t_1) < 0; V_{CO} = 0; D_2 \text{ conducts.} \end{cases} \tag{1}$$

Mode 3 (t_2-t_3): Switches S_1, S_2, and S_5 conducts. V_{C_r} and V_{CO} both rise in this mode, keeping both the diodes D_1 starts conducting and D_2 reverse biased. However, the current I_{L_1} is very low due to coupling effect in inductors

$$\begin{cases} V_{C_r}(t-t_2) = \frac{V_{\text{in}}}{n}[1-\cos\omega_0(t-t_2)] + Z_0 I_{L_r}(t_2) \\ \sin\omega_0(t-t_2) \\ I_{L_r}(t-t_2) = I_{L_r}(t_2)\cos\omega_0(t-t_2) + \frac{V_{\text{in}}}{nZ_0}\sin\omega_0(t-t_2) \\ V_{C_r}(t-t_2) > 0. \end{cases} \tag{2}$$

Mode 4 (t_3-t_4): Diode D_1 continue to conduct significant current as voltage V_{C_r} is greater than voltage V_{CO}

$$\begin{cases} V_{C_r}(t-t_3) = \frac{V_{\text{in}}}{n} - \left[\frac{V_{\text{in}}}{n} - V_{C_r}(t_3)\right] \cos\omega_0(t-t_3) \\ +Z_0 I_{L_r}(t_3)\sin\omega_0(t-t_3) \\ I_{L_1}(t-t_3) = \frac{V_{C_r}(t-t_3) - V_{CO}}{j\omega L_{1e}} \\ V_{C_r}(t-t_3) > V_{CO}; D_1 \text{ conducts.} \end{cases} \tag{3}$$

Mode 5 (t_4-t_5): Switches S_1 and S_2 conducts and switch S_5 turns ON at zero voltage. The primary current I_{pri} decays and switches S_1, S_2, and S_5 turn-OFF at the end of this mode. D_1 continues to conduct as V_{C_r} is still greater than V_{CO}

$$\begin{cases} V_{C_r}(t-t_4) = \frac{V_{\text{in}}}{n} - [\frac{V_{\text{in}}}{n} - V_{C_r}(t_4)]\cos\omega_0(t-t_4) \\ I_{L_r}(t-t_4) = \frac{\frac{V_{\text{in}}}{n} - V_{C_r}(t_4)}{Z_0}\sin\omega_0(t-t_4) \\ I_{L_r}(t_4) = 0. \end{cases} \tag{4}$$

Mode 6 (t_5-t_6): Switches S_3, S_4, and S_6 are fired at the beginning of this mode. The primary current I_{pri} is still positive and decays to zero at the end of this mode. The body diodes of switches S_3 and S_4 carry current I_{pri} creating conditions for zero voltage turn-ON

$$\begin{cases} V_{C_r}(t-t_5) = \frac{-V_{\text{in}}}{n} - [\frac{-V_{\text{in}}}{n} - V_{C_r}(t_5)]\cos\omega_0(t-t_5) \\ +Z_0 I_{L_r}(t_5)\sin\omega_0(t-t_5) \\ I_{L_r}(t-t_5) = I_{L_r}(t_5)\cos\omega_0(t-t_5) + \frac{\frac{-V_{\text{in}}}{n} - V_{C_r}(t_5)}{Z_0} \\ \sin\omega_0(t-t_5). \end{cases} \tag{5}$$

Mode 7 (t_6-t_7): Switches S_3 and S_4 turn ON at zero voltage as I_{pri} makes reversal. The capacitor voltage V_{C_r} falls below V_{CO} turning OFF diode D_1 at the end of the mode.

Mode 8 (t_7-t_8): Voltage V_{C_r} begins to drop after time instant t_7. As V_{C_r} equals V_{CO} diode D_1 is reverse biased and D_2 begins to conduct but magnitude of current is small.

Mode 9 (t_8-t_9): At time instant t_8, V_{CO} is zero as D_2 get forward biased. With D_2 and S_6 conducting I_{L_1} start to build up in negative direction

$$\begin{cases} I_{L_1}(t-t_8) = \frac{V_{C_r}(t-t_8)}{j\omega L_{1e}} \\ V_{C_r}(t_8) = 0, V_{CO} = 0; D_2 \text{ conducts.} \end{cases} \tag{6}$$

Mode 10 (t_9-t_{10}): Switches S_3 and S_4 conducts, switch S_6 turns-ON at zero voltage and diode D_2 is conducting. Switches

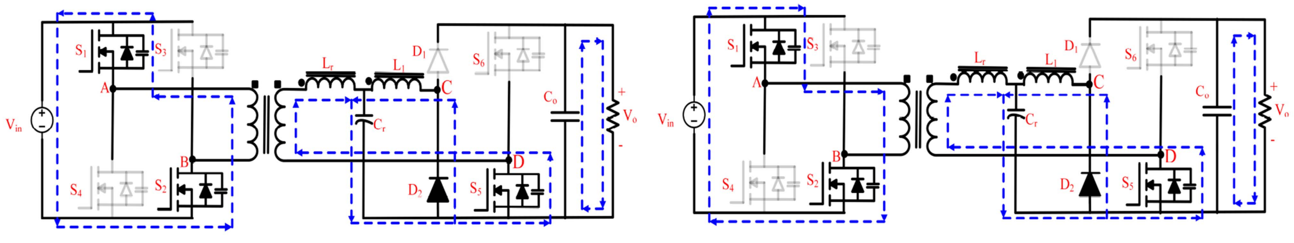

Mode 1 (t_0-t_1)

Mode 2 (t_1-t_2)

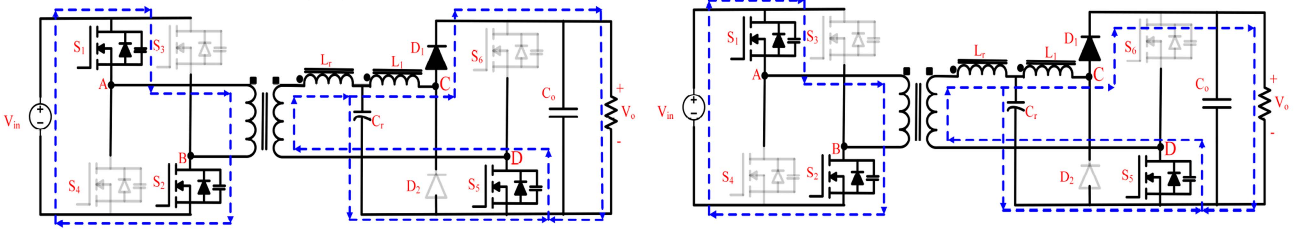

Mode 3 (t_2-t_3)

Mode 4 (t_3-t_4)

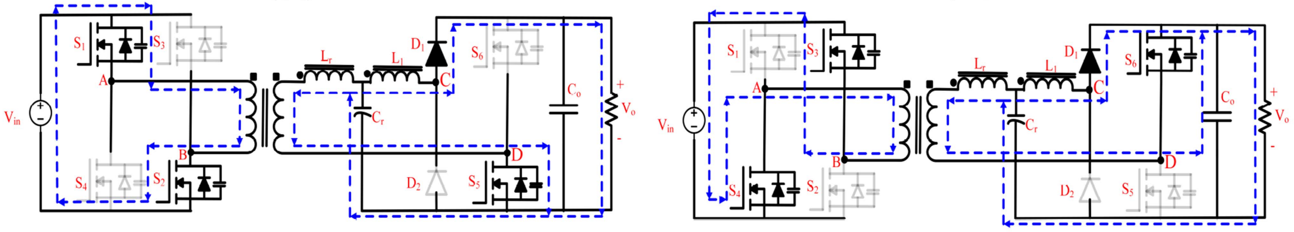

Mode 5 (t_4-t_5)

Mode 6 (t_5-t_6)

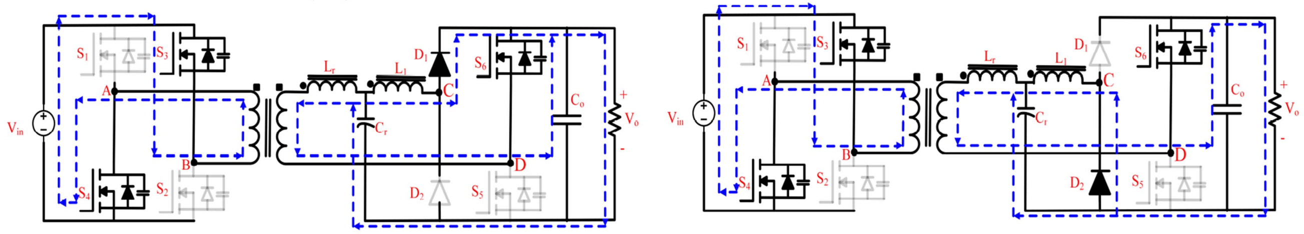

Mode 7 (t_6-t_7)

Mode 8 (t_7-t_8)

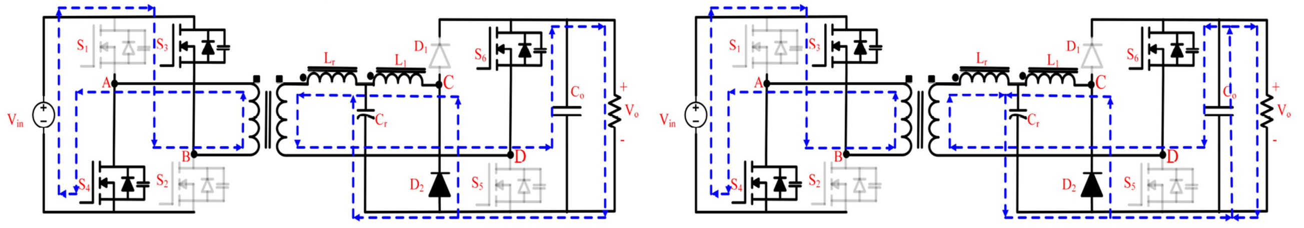

Mode 9 (t_8-t_9)

Mode 10 (t_9-t_{10})

Fig. 3. Operating modes of proposed DC–DC resonant converter in charging operation.

S_1, S_2, and S_5 are fired and switches S_3, S_4, and S_6 are turned OFF at the end of this mode. After this mode, switching cycle repeats

$$\begin{cases} V_{C_r}(t-t_9) = \frac{-V_{\text{in}}}{n}[1-\cos\omega_0(t-t_9)]) \\ I_{L_r}(t-t_9) = -\frac{V_{\text{in}}}{nZ_0}\sin\omega_0(t-t_9) \\ I_{L_r}(t_9) = 0. \end{cases} \tag{7}$$

At the end of this mode, body diodes switch S_1 and S_2 starts conducting leading to zero voltage turn-ON for S_1 and S_2.

III. TRANSFORMER AND INDUCTOR INTEGRATION

A. *Integrated Transformer Structure*

The winding arrangement of the integrated magnetics transformer and inductors is shown in Fig. 4. A EE core has been used to design a integrated structure. The transformer windings have been wound on the middle limb of the core and the inductor windings are wound on the outer two legs of the core. Inductor L_r is wound on leg I and inductor L_1 on leg II. The windings have been arranged such that the flux in leg I assists flux in leg II.

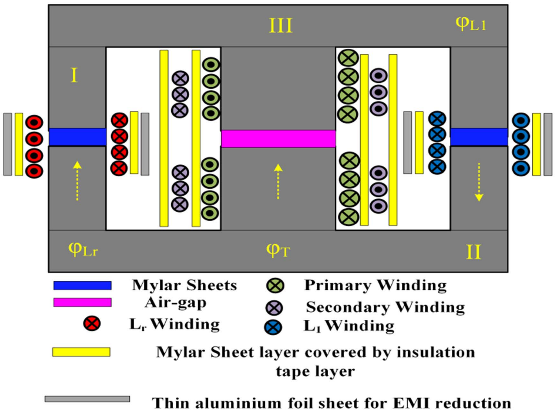

Fig. 4. Schematic diagram showing winding arrangement of the two inductors and transformer on a EE core.

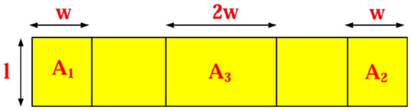

Fig. 5. Top view of EE core.

The inductors act as coupled inductors wound on the same core. ϕ_{L_r} is the flux due to resonant inductor L_r alone, ϕ_T represent net flux in leg III due to the effect of primary and secondary windings and ϕ_{L_1} indicates flux due to winding L_1 alone. ϕ_1, ϕ_2, and ϕ_3 are the net fluxes produced by windings under the joint action of legs I–III, respectively. Cross-sectional areas of the core remain same in the legs I and II whereas cross sectional area of leg III is double that of the areas of leg I and leg II. Air-gap, l_g is same in all the three legs of the EE core.

As shown in Fig. 5, length l of all the three legs of the core remains same but width of middle leg is double of other two legs. So, relation between the areas of all the three legs can be written as

$$2A_1 = A_3 = 2A_2. \tag{8}$$

As reluctance of a leg is given by

$$\mathcal{R} = \frac{l}{\mu A}. \tag{9}$$

Hence, reluctances $\mathcal{R}_1$ of leg I and $\mathcal{R}_2$ of leg II are equal whereas reluctance $\mathcal{R}_3$ on the middle leg is half of side legs of the core. The equivalent magnetic circuit of the integrated structure is shown in Fig. 15. N_{pri} represent number of turns on the primary winding and N_{sec} represent number of turns on secondary winding, respectively. N_{L_r} and N_{L_1} are the number of turns of inductor L_r and L_1 and their corresponding mmfs are $N_{L_r}i_{L_r}$ and $N_{L_1}i_{L_1}$. $N_{\text{pri}}i_{\text{pri}}$ and $N_{\text{sec}}i_{\text{sec}}$ are primary side and secondary side mmf. The windings on the same core exhibit coupling coefficients with each other (derived in Appendix). Hence, the inductor windings on the core are coupled with each other with a coupling coefficient of 0.33. So, *LCL-T* network in this case is a coupled *LCL-T* type resonant network.

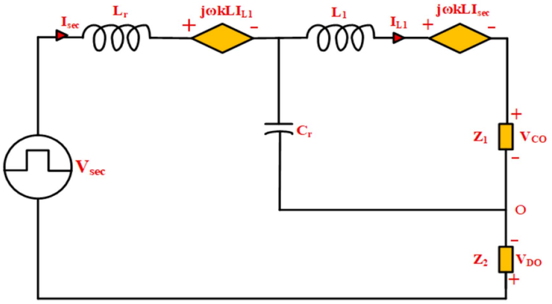

Fig. 6. Equivalent circuit diagram.

B. Electrical Circuit Analysis

The equivalent circuit diagram for the converter can be represented as shown in Fig. 6 below. L_r and L_1 are inductors with mutual inductance $M = k\sqrt{L_rL_1}$, C is the shunt capacitor, if $L_r = L_1 = L$ and coupling coefficient is k, then mutual inductance can be written as $M = kL$. Applying Kirchoff voltage law (KVL) in the equivalent ciruit diagram, the following equations can be written as:

$$\begin{cases} V_{\text{sec}} = (j\omega L + \frac{1}{j\omega C_r} + Z_2)i_{\text{sec}} - (j\omega kL + \frac{1}{j\omega C_r})i_{L_1} \\ i_{L_1} = \frac{\frac{1}{j\omega C_r}}{j\omega L + \frac{1}{j\omega C_r} + Z_1} i_{\text{sec}}. \end{cases} \tag{10}$$

The resonance condition for the network can be written as

$$\frac{-1}{j\omega C_r} = j\omega L \tag{11}$$

using the resonance condition given in (11), (10) can be written as

$$\begin{cases} V_{\text{sec}} = Z_2 i_{\text{sec}} - (j\omega kL + \frac{1}{j\omega C_r})i_{L_1} \\ i_{L_1} = \frac{1}{j\omega C_r Z_1} i_{\text{sec}}. \end{cases} \tag{12}$$

Hence, the input impedance of the equivalent circuit diagram can be realized as

$$Z_{\text{in}} = \frac{\omega^2 C_r^2 Z_1 Z_2 - k + 1}{\omega^2 C_r^2 Z_1}. \tag{13}$$

It can be deduced from (13) that the input impedance is dependent upon the nature of Z_1 and Z_2. If Z_1 and Z_2 are resistive in nature then the input impedance is also resistive. As dependent sources are present in the electrical equivalent circuit, equivalent impedance across Z_2 can be written as

$$Z_2 = \frac{(1-k^2)}{\omega^2 C_r^2 Z_1}. \tag{14}$$

The mode of the converter changes when both the impedance Z_1 and Z_2 are equal. This point is regarded as transition point. As both the impedance are equal, (14) can be rewritten as

$$\begin{cases} Z_1^2 = \frac{(1-k^2)}{\omega^2 C_r^2} \\ Z_1 = Z_2 = \frac{\sqrt{(1-k^2)}}{\omega C_r}. \end{cases} \tag{15}$$

Rated value of load at which the charging mode changes from CC to CV can be written as

$$R_t = \frac{V_{\text{out}}}{I_{\text{out}}} = \frac{400\ \text{V}}{5\ \text{A}} = 80\ \Omega. \tag{16}$$

TABLE I
COMPARISON OF DISCRETE AND INTEGRATED MAGNETIC STRUCTURES

item	Discrete Magnetics			Integrated Magnetics	
	Core	**Volume**	**Weight**	**Volume**	**Weight**
Inductor L_r	EI3313	7.901 cm^3	39.5 gm	78.2 cm^3	385 gm
Inductor L_1	EI3313	7.901 cm^3	39.5 gm		
Transformer	EE6527	78.200 cm^3	385 gm		
Total		94.002 cm^3	464 gm	78.2 cm^3	385 gm

TABLE II
DESIGN SPECIFICATIONS OF PROPOSED CONVERTER

Parameter	**Value**
Input Voltage, V_{in}	400 V
Output Voltage, V_{out}	200–400 V
Rated Power, P_{out}	2 KW
Resonant switching frequency, f_s	100 kHz

TABLE III
KEY PARAMETERS OF THE PROTOTYPE

Component	**Part Number**
$S_1 - S_6$	C2M0040120D
Transformer	EE6527 core, L_{pri} = 500 μH N_{pri}:N_{sec}= 2:1
L_r,L_1	27.33 μH
C_r	92.67 nF
$D_1 - D_2$	C3D03060A
C_{out}	470 $\mu F/450\ V$
Gate Driver	UCC21750 (Texas Instruments)

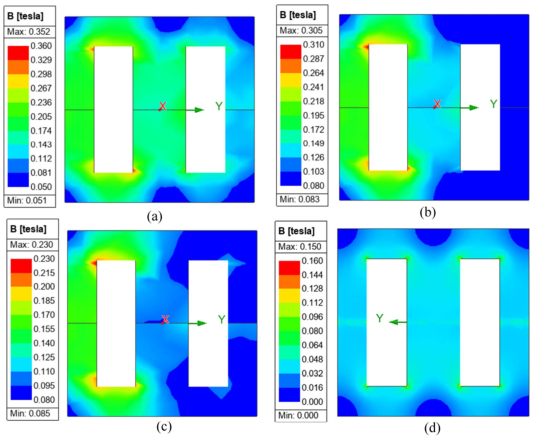

Fig. 7. Peak flux density distribution of integrated transformer under the conditions where $V_{\text{in}} = 400$ V. (a) $P_o = 2000$ W, (b) $P_o = 1500$ W, (c) $P_o = 1000$ W, and (d) discrete transformer with input voltage excitation $V_{\text{in}} = 400$ V

At transition point Z_1 and Z_2 both are equal and resistive. Hence, input impedance of the equivalent circuit is also resistive. So, the equivalent resistance is combination of two legs operating in parallel, which can be represented as

$$\left\{ Z_1||Z_2 = \tfrac{2}{\pi^2} R_t \& \quad \tfrac{2}{\pi^2} R_t = \frac{\sqrt{(1-k^2)}}{\omega C_r}. \right. \tag{17}$$

The values of resonant capacitor and inductor can be calculated using (11) and (17). The expression for voltages V_{CO} and V_{DO} can be written as

$$\begin{cases} V_{CO} = \frac{\omega C_r Z_1}{Z_1 Z_2 \omega^2 C_r^2 - k + 1} V_{\text{sec}} \\ V_{DO} = \frac{Z_1 Z_2 \omega^2 C_r^2}{Z_1 Z_2 \omega^2 C_r^2 - k + 1} V_{\text{sec}} \\ i_{\text{out}} = \frac{4 V_{\text{in}}}{n\pi^2 (Z_1 Z_2 \omega^2 C_r^2 - k + 1)} (\omega C_r - \frac{1-k^2}{Z_2}). \end{cases} \tag{18}$$

Equation (18) shows that while voltage V_{DO} is constant, voltage V_{CO} is dependent on Z_1. Z_2 is high when i_{out} is high. According to (14), with larger Z_2, Z_1 should be smaller in order to maintain the Z_1 Z_2 product constant. The voltage V_{CO} increases as Z_1 increases and, as a result, Z_2 decreases. With decreasing Z_2 and increasing Z_1 converter maintains small drop in load current but significant rise in load voltage. At the transition point both Z_1 and Z_2 are equal. Following the transition point, Z_1 increases to show that the output voltage has reached the saturation point and Z_2 decreases to show a decline in load current.

Rate of decay of load current is higher after the transition point whereas variation in output voltage is very small. This indicates charging profile transition of the converter from CC to CV. The current I_{L_1} is not zero even after the mode transition point because of coupling effect but the magnitude of this current is very feeble as currents causing coupling effects are also decreasing. Also, the coupling coefficients between the windings are not very encouraging to lead to significant current in the circuit.

C. ZVS Boundary Analysis

To achieve soft switching, the stored charge-based energy criteria including the parasitic capacitance have been used [22], the expression of net impedance referred to the primary side and the phase between voltage and current can be written as

$$\begin{cases} \frac{1}{2} L_m i_{\text{pri}}^2 \geq C_{Q,\text{eq}}(V_{\text{in}}) V_{\text{in}}^2 + \frac{1}{2} C_{\text{par}} V_{\text{in}}^2 \\ \quad Z_{\text{net}} = j\omega L_m || n^2 Z_{\text{in}} \quad \text{and} \quad \phi = \tan^{-1}\left(\frac{n^2 Z_{\text{in}}}{\omega L_m}\right) \\ |Z_{\text{net}}| = \sqrt{\frac{(\omega^2 L_m^2 n^2 Z_{\text{in}}^2)^2 + (\omega L_m n^4 Z_{\text{in}}^2)^2}{(n^2 Z_{in}^2)^2 + (\omega L_m)^2}} \end{cases} \tag{19}$$

where Z_{in} is input impedance, C_{par} is the parasitic capacitance, and $C_{Q,\text{eq}}(V_{\text{in}})$ is equivalent capacitance of switches as a function of input voltage in the circuit. So, the condition of soft switching can be derived as

$$L_m \geq \sqrt[3]{\frac{\pi^2 [C_{Q,\text{eq}}(V_{\text{in}}) + C_{\text{par}}]}{16 \omega^2 n^4 Z_{\text{in}}^2}} \quad \text{and} \quad \phi = \tan^{-1}(\frac{n^2 Z_{\text{in}}}{\omega L_m}) < 0. \tag{20}$$

It is to be noted that due to coupling, mutual inductance affects the effective resonant behavior improving ZVS at light load condition. Primary side inductance has been kept large enough to sustain charging and discharging of MOSFET gate.

IV. RESULTS AND DISCUSSION

A. Comparison of Integrated and Discrete Magnetic Structure

In order to explore flux distribution inside the core of integrated magnetic structure, ANSYS maxwell 3-D FEA is performed. Input voltage was set to the integrated transformer is 400 V. Fig. 7(a)–(c) shows peak flux density distribution inside the core of integrated transformer for different power outputs. Left column of the core represents higher density than the right side column of the EE core. This nonuniform distribution of flux density indicates that fluxes add up in left column at peak power

TABLE IV
COMPARISON BETWEEN PROPOSED CONVERTER AND OTHER CONVERTERS

Reference	**[5]**	**[6]**	**[7]**	**[20]**	**[21]**	**Proposed**
Resonant Network	LLC	CLL	LLC	LCL-T	CLCLC	LCL-T
Magnetic Integration	YES	YES	YES	NO	NO	YES
Magnetic Components	1	1	1	3	3	1
Rated Power	400 W	400 W	350 W	1 kW	200 W	2 kW
Output Voltage	48 V	20 V	19.5 V	250–400	75 V	200–400 V
Efficiency	96.3%	97.1%	95.26%	96.7%	95%	98.15%
Switching Frequency	350 kHz	500 kHz	800 kHz	100 kHz	100 kHz	100 kHz

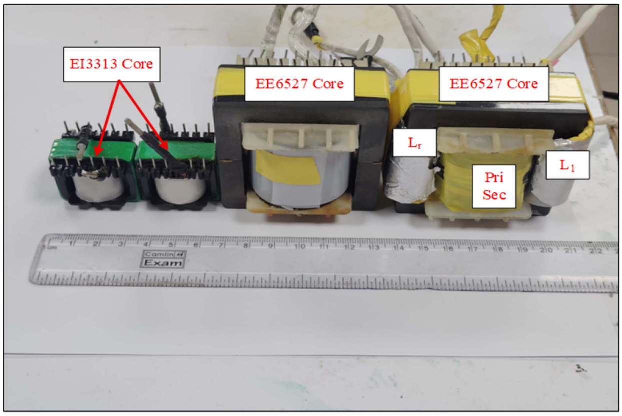

Fig. 8. Discrete magnetic structures and integrated magnetic structure.

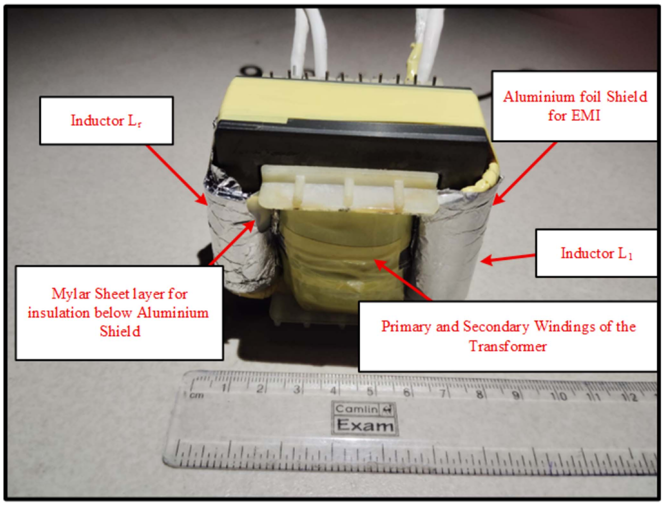

Fig. 9. Integrated magnetic structure.

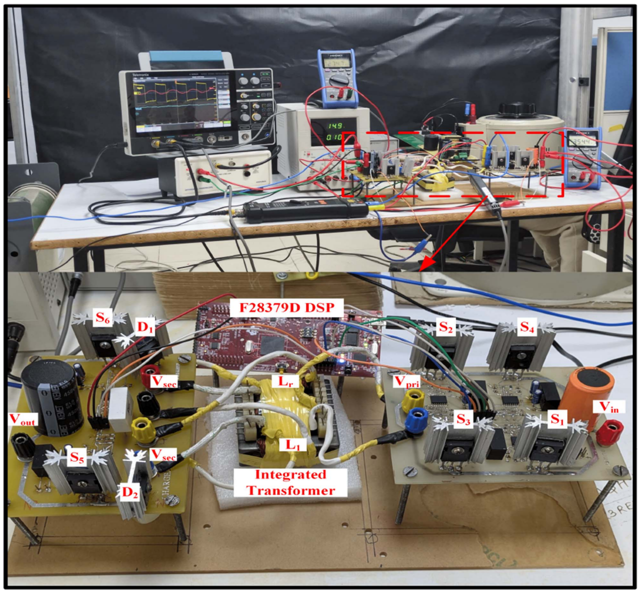

Fig. 10. Hardware setup of the proposed converter.

output as the current is significant in both the windings. As the current starts to drop, the peak flux density also decreases but flux distribution is still nonuniform. The field distribution in Fig. 7(d) is uniform as both the columns of the discrete transformer offer equal reluctance. Fig. 8 shows discrete physical structure of transformer on EE6527 core and two inductors on EI3313 core along with integrated transformer.

B. Hardware Validation

A 2-kW laboratory prototype with the specification given in Table II is tested to verify the effectiveness of the proposed converter. AWG 26 wire gauge has been chosen at 100 kHz operating frequency in the design of transformer and inductor windings. The number of parallel conductors has been used in order to accommodate the rated currents in all the windings. In order to meet isolation, every leg winding structure is covered by mylar sheet and complete magnetic structure is tightened by insulation tape. Transformer primary windings are also separated by mylar sheets. Thin aluminum foils wound on the side columns over insulation tape to contain electromagnetic interference (EMI) originating from the side columns. Fig. 9 shows complete integrated magnetic assembly with annotations. In order to verify the performance of the converter, battery has been modeled as a dc passive load. Fig. 10 shows the hardware setup for the proposed converter.

Fig. 11(a) shows primary current I_{pri} lagging zero crossing in reference primary voltage V_{pri}. This indicates the body diodes of switches S_1 and S_2 are carrying current I_{pri} ensuring zero voltage turn-ON for the switches S_1 and S_2. Similarly, ZVS can be validated at other load values also in Fig. 11(b), 11(c). Voltages V_{CO} and V_{DO} are shown with current I_{L_1} in Fig. 11(d)–(f). As it is evident from the Fig. 11(d) that current I_{L_1} is maximum and keep on decreasing with the decrease in load value. As shown in Fig. 14 peak efficiency is observed at the peak load value.

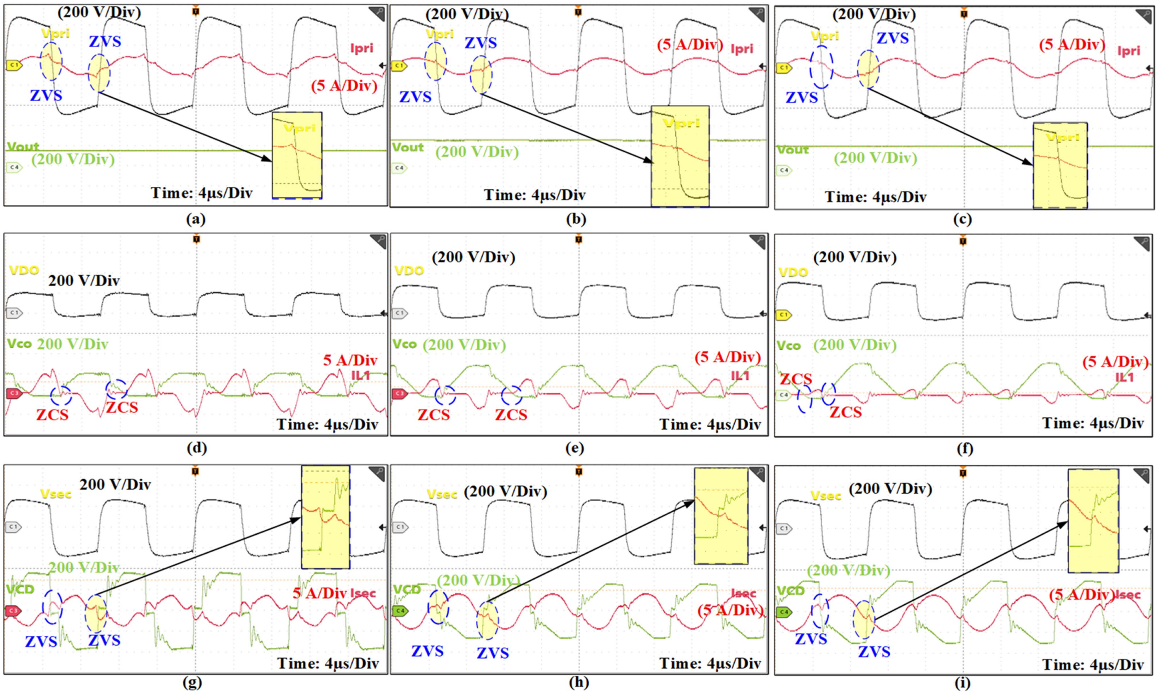

Fig. 11. Experimental waveforms of the proposed converter, V_{pri}, I_{pri}, and V_{out} at loads (a) 1152 W, (b) 1620 W, (c) 838 W, V_{CO}, I_{L_1}, and V_{DO} at loads, (d) 1152 W, (e) 1620 W, (f) 838 W, V_{sec}, I_{sec}, andV_{CD} at loads, (g) 1152 W, (h) 1620 W, and (i) 838 W.

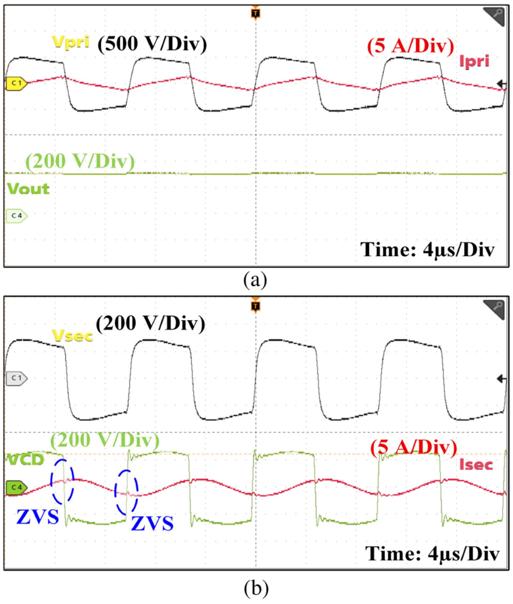

Fig. 12. (a) V_{pri}, I_{pri}, and V_{out} and (b) V_{sec}, I_{sec}, and V_{CD} at 136.62 W load.

The load current beyond this point drops significantly whereas no significant change is observed in the output voltage. Highest efficiency is achieved at peak load when Z_1 and Z_2 are equal. The input impedance offered by the equivalent electrical circuit is resistive as shown in (15). Beyond transition point, output voltage reaches almost rated voltage and load current continue to drop with decreasing load. As the efficiency curve shown in Fig. 14 indicates that due to drop in load current, output power

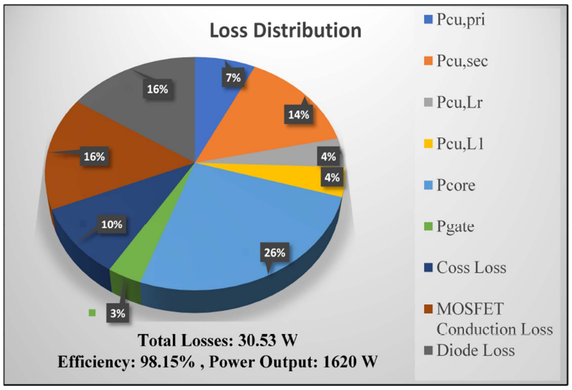

Fig. 13. Loss distribution in the converter at peak efficiency.

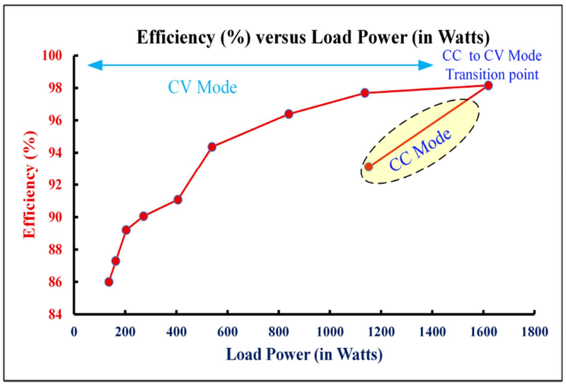

Fig. 14. Efficiency versus load plot for charging mode operation.

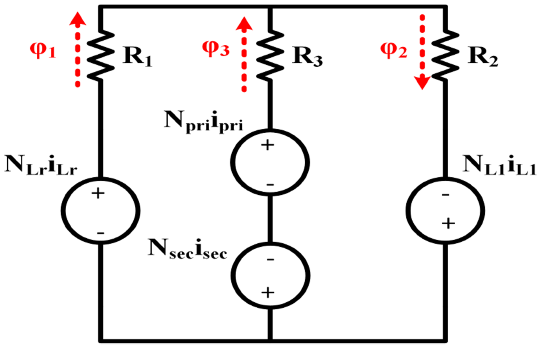

Fig. 15. Magnetic equivalent circuit.

and efficiency of the converter are decreasing. This peak load is the charging mode transition point from CC to CV according to the calculated values. For discrete magnetic converter, current I_{L_1} beyond this point should be zero but due to presence of coupling between the integrated transformer windings current I_{L_1} is present and decaying after the transition point which can be observed from Fig. 11(d)–(f) with decreasing load output.

Voltages V_{sec} and V_{CD} are shown with current I_{sec} in Fig. 11(g)–(i). As it is evident from the figures that body diodes of switches conduct for most of the time and and switch S_5 and S_6 conduct for a short duration and hence, switches turn-ON at zero voltage. The spike observed at the switching point in I_{sec} is the short duration turn-ON of the switches. So switches on the secondary side also observe soft switching over the load range. Minimum output power attained by the converter is 136.62 W at an efficiency of 86.004%. This indicates the light load efficiency of the converter. The efficiency and output waveforms at light load are shown in Figs. 12–14 shows loss distribution in the converter at peak efficiency.

V. CONCLUSION

A *LCL-T*-based dc–dc converter with integrated magnetics is presented in this article. The converter electrical circuit analysis, magnetic circuit analysis, and design specifications have been discussed in detail. A prototype of 2 kW has been tested and verified in the lab with 400 V input and 200–400 V output range. The converter achieves peak efficiency of 98.15%. The converter achieves inherent mode transition from CC to CV without any control and sensing. Magnetic integration reduces volume of the magnetic components by 20.2% and weight of the components by 17.02%. Hence, the proposed integrated transformer offers higher power density than the discrete components.

APPENDIX
MAGNETIC CIRCUIT ANALYSIS OF INTEGRATED MAGNETICS TRANSFORMER

As shown in Fig. 15 The magnetic fluxes generated in each column can be written as

$$\begin{cases} \phi_{L_r} &= \frac{N_{L_r} i_{L_r}}{R_1+R_2||R_3} = \frac{N_{L_r} i_{L_r}(R_2+R_3)}{\Delta} \\ \phi_{L_1} &= \frac{N_{L_1} i_{L_1}}{R_2+R_1||R_3} = \frac{N_{L_1} i_{L_1}(R_1+R_3)}{\Delta} \\ \phi_T &= \frac{\Phi}{R_3+R_1||R_2} = \frac{\Phi(R_1+R_2)}{\Delta} \end{cases} \tag{21}$$

where $\Delta = R_1R_2 + R_2R_3 + R_3R_1$ and $\Phi = (N_{\text{pri}} i_{\text{pri}} - N_{\text{sec}} i_{\text{sec}}$. The joint action of fluxes in the three legs are as

$$\begin{cases} \phi_1 &= \phi_{L_r} + \phi_{L_1} \frac{R_3}{R_3+R_1} - \phi_T \frac{R_2}{R_1+R_2} \\ \phi_2 &= \phi_{L_r} \frac{R_3}{R_3+R_2} + \phi_{L_1} + \phi_T \frac{R_1}{R_1+R_2} \\ \phi_3 &= -\phi_{L_r} \frac{R_2}{R_2+R_3} + \phi_{L_1} \frac{R_1}{R_1+R_3} + \phi_T \end{cases} \tag{22}$$

putting (21) in (22), we get

$$\begin{cases} \phi_1 = N_{L_r} I_{L_r} \frac{(R_2+R_3)}{\Delta} + N_{L_1} I_{L_1} \frac{R_3}{\Delta} - \Phi \frac{R_2}{\Delta} \\ \phi_2 = N_{L_r} I_{L_r} \frac{R_3}{\Delta} + N_{L_1} I_{L_1} \frac{(R_1+R_3)}{\Delta} - \Phi \frac{R_1}{\Delta} \\ \phi_3 = -N_{L_r} i_{L_r} \frac{R_2}{\Delta} - N_{L_1} i_{L_1} \frac{R_1}{\Delta} + \Phi \frac{(R_1+R_2)}{\Delta}. \end{cases} \tag{23}$$

So, voltages can be written as

$$\begin{cases} V_{\text{pri}} = N_{\text{pri}} \frac{d\phi_3}{dt}; V_{\text{sec}} = -N_{\text{sec}} \frac{d\phi_3}{dt} \\ V_{L_r} = N_{L_r} \frac{d\phi_1}{dt}; V_{L_1} = N_{L_1} \frac{d\phi_2}{dt}. \end{cases} \tag{24}$$

According to (22)–(24), the relationship between the winding voltages and currents of IM can be written as

$$\begin{bmatrix} V_{\text{pri}} \\ V_{\text{sec}} \\ V_{L_r} \\ V_{L_1} \end{bmatrix} = \begin{bmatrix} L_{\text{pri}} & M_{\text{prisec}} & M_{\text{pri}L_r} & M_{\text{pri}L_1} \\ M_{\text{secpri}} & L_{\text{sec}} & M_{\text{sec}\,L_r} & M_{\text{sec}\,L_1} \\ M_{L_r\text{pri}} & M_{L_r\,\text{sec}} & L_{L_r\,\text{sec}} & -M_{L_rL_1} \\ M_{L_1\text{pri}} & M_{L_1\,\text{sec}} & M_{L_1L_r} & L_{L_1} \end{bmatrix} \begin{bmatrix} \frac{di_{\text{pri}}}{dt} \\ \frac{di_{\text{sec}}}{dt} \\ \frac{di_{L_r}}{dt} \\ \frac{di_{L_1}}{dt} \end{bmatrix} \tag{25}$$

where $M_{\text{pri}L_r}$, $M_{\text{pri}L_1}$, $M_{\text{sec}\,L_r}$, $M_{\text{sec}\,L_1}$, and $M_{L_rL_1}$ are mutual inductance between primary winding-L_r, primary winding-L_1, secondary winding-L_r, secondary winding-L_1, inductor L_r-L_1

$$\begin{cases} L_{\text{pri}} &= N_p^2 \frac{(\mathcal{R}_1+\mathcal{R}_2)}{\Delta}; L_{\text{sec}} = N_s^2 \frac{(\mathcal{R}_1+\mathcal{R}_2)}{\Delta} \\ L_{L_r} &= N_{L_r}^2 \frac{(\mathcal{R}_2+\mathcal{R}_3)}{\Delta}; L_{L_1} = N_{L_1}^2 \frac{(\mathcal{R}_1+\mathcal{R}_3)}{\Delta} \\ M_{\text{prisec}} &= -N_{\text{pri}} N_{\text{sec}} \frac{(\mathcal{R}_1+\mathcal{R}_2)}{\Delta}; M_{L_rL_1} = N_{L_r} N_{L_1} \frac{\mathcal{R}_3}{\Delta} \\ M_{\text{pri}L_r} &= -N_{\text{pri}} N_{L_r} \frac{\mathcal{R}_2}{\Delta}; M_{\text{pri}L_1} = N_{\text{pri}} N_{L_1} \frac{\mathcal{R}_1}{\Delta} \\ M_{\text{sec}\,L_r} &= N_{\text{sec}} N_{L_r} \frac{\mathcal{R}_2}{\Delta}; M_{\text{sec}\,L_1} = -N_{\text{sec}} N_{L_1} \frac{\mathcal{R}_1}{\Delta}. \end{cases} \tag{26}$$

According to (26), we can calculate all the coupling coefficients as follows:

$$\begin{cases} K_{\text{prisec}} = \frac{M_{\text{prisec}}}{\sqrt{L_{\text{pri}} L_{\text{sec}}}} = -1; K_{L_rL_1} = \frac{M_{L_rL_1}}{\sqrt{L_r L_1}} = 0.33 \\ K_{\text{pri}L_r} = \frac{M_{\text{pri}} L_r}{\sqrt{L_{\text{pri}} L_r}} = -0.577; K_{\text{pri}L_1} = \frac{M_{\text{pri}} L_1}{\sqrt{L_{\text{pri}} L_1}} = 0.577 \\ K_{\text{sec}\,L_r} = \frac{M_{\text{sec}} L_r}{\sqrt{L_{\text{sec}} L_r}} = -0.577; K_{\text{sec}\,L_1} = \frac{M_{\text{sec}} L_1}{\sqrt{L_{\text{sec}} L_1}} = 0.577. \end{cases} \tag{27}$$

REFERENCES

[1] S. Habib, M. M. Khan, F. Abbas, L. Sang, M. U. Shahid, and H. Tang, "A comprehensive study of implemented international standards, technical challenges, impacts and prospects for electric vehicles," *IEEE Access*, vol. 6, pp. 13866–13890, 2018.

[2] J. W. M. Soares and A. A. Badin, "An interleaved PFC boost converter with soft commutations and voltage follower characteristics," *IEEE Trans. Ind. Electron.*, vol. 69, no. 7, pp. 6732–6740, Jul. 2022.

[3] M. Borage, K. Nagesh, M. Bhatia, and S. Tiwari, "Resonant immittance converter topologies," *IEEE Trans. Ind. Electron.*, vol. 58, no. 3, pp. 971–978, Mar. 2011.

[4] H. Wouters and W. Martinez, "Integrated inductor-transformers for high-frequency converters: An overview," *IEEE Trans. Power Electron.*, vol. 40, no. 9, pp. 13157–13176, Sep. 2025.

[5] S. Gao and Z. Zhao, "Magnetic integrated LLC resonant converter based on independent inductance winding," *IEEE Access*, vol. 9, pp. 660–672, 2021.

[6] Y. Liu, H. Wu, J. Zou, Y. Tai, and Z. Ge, “*CLL* resonant converter with secondary side resonant inductor and integrated magnetics,” *IEEE Trans. Power Electron.*, vol. 36, no. 10, pp. 11316–11325, Oct. 2021.

[7] C.-W. Park and S.-K. Han, “Analysis and design of an integrated magnetics planar transformer for high power density LLC resonant converter,” *IEEE Access*, vol. 9, pp. 157499–157511, 2021.

[8] M. D’Antonio, S. Chakraborty, and A. Khaligh, “Planar transformer with asymmetric integrated leakage inductance using horizontal air gap,” *IEEE Trans. Power Electron.*, vol. 36, no. 12, pp. 14014–14028, Dec. 2021.

[9] S. A. Ansari, J. N. Davidson, and M. P. Foster, “Fully-integrated transformer with asymmetric primary and secondary leakage inductances for a bidirectional resonant converter,” *IEEE Trans. Ind. Appl.*, vol. 59, no. 3, pp. 3674–3685, May/Jun. 2023.

[10] F. Li, L. Wang, and L. Yu, “A novel integrated matrix magnetics for isolated single-stage DC–DC converter,” *IEEE Trans. Power Electron.*, vol. 37, no. 10, pp. 12380–12390, Oct. 2022.

[11] H. Wu, Y. Zhang, and Z. Li, “Hybrid resonant converter-based 8:1 bus converter with 3.5 kW/in^3 and 98.6%-efficient for 48 V data-center power systems,” *IEEE Trans. Power Electron.*, vol. 39, no. 1, pp. 36–41, Jan. 2024.

[12] J. Guo, H. Wang, G. Xu, H. Han, and M. Su, “Dual-transformer-based DAB converter with controllable integrated inductances,” *IEEE Trans. Power Electron.*, vol. 39, no. 5, pp. 6376–6390, May 2024.

[13] L. Zhao et al., “An integrated 6.78-MHz class Φ_2 converter using bifurcation phenomenon of resonance between the isolation transformer,” *IEEE Trans. Power Electron.*, vol. 39, no. 10, pp. 12003–12007, Oct. 2024.

[14] Z. Guo, H. Yang, and G. Cao, “A structure and design method for magnetic integration of current-fed dual active bridge DC–DC converters,” *IEEE Trans. Power Electron.*, vol. 40, no. 8, pp. 10594–10608, Aug. 2025.

[15] J. Guo, H. Wang, G. Xu, Y. Sun, and M. Su, “Magnetic integration with controllable leakage inductance and unbalanced current suppression for CF DAB converter based on single EE core,” *IEEE Trans. Power Electron.*, vol. 40, no. 10, pp. 15562–15571, Oct. 2025.

[16] Z. Li, E. Hsieh, Q. Li, and F. C. Lee, “High-frequency transformer design with medium-voltage insulation for resonant converter in solid-state transformer,” *IEEE Trans. Power Electron.*, vol. 38, no. 8, pp. 9917–9932, Aug. 2023.

[17] E. de Jong, B. Ferreira, and P. Bauer, “Toward the next level of PCB usage in power electronic converters,” *IEEE Trans. Power Electron.*, vol. 23, no. 6, pp. 3151–3163, Nov. 2008.

[18] M. Borage, S. Tiwari, and S. Kotaiah, “LCL-T resonant converter with clamp diodes: A novel constant-current power supply with inherent constant-voltage limit,” *IEEE Trans. Ind. Electron.*, vol. 54, no. 2, pp. 741–746, Apr. 2007.

[19] S. Wang, Y. Liu, and X. Wang, “Resonant converter for battery charging applications with CC/CV output profiles,” *IEEE Access*, vol. 8, pp. 54879–54886, 2020.

[20] X. Li, H. Ma, S. Ren, J. Yi, S. Lu, and Q. Feng, “A novel LCL resonant converter with inherent CC-CV output for on-board chargers of plug-in electric vehicles,” *IEEE Trans. Power Electron.*, vol. 38, no. 4, pp. 4212–4217, Apr. 2023.

[21] R. Wang, S. Hu, X. Li, L. Zhong, W. Chen, and H. Wen, “A *CLCLC*-type immittance resonant DAB converter with dual unbalanced modulation for electric vehicle charger,” *IEEE Trans. Transport. Electrific.*, vol. 11, no. 1, pp. 4504–4514, Feb. 2025.

[22] M. Kasper, R. Burkart, G. Deboy, and J. W. Kolar, “ZVS of power MOSFETs revisited,” *IEEE Trans. Power Electron.*, vol. 31, no. 12, pp. 8063–8067, Dec. 2016.

Akash Deo (Student Member, IEEE) received the B.E. degree in electronics and communication engineering from Government Engineering College, Bhopal, India, in 2010, and the M.Tech. degree in power electronics and ASIC design from the Motilal Nehru National Institute of Technology, Allahabad, India, in 2013. He is currently working toward the Ph.D. degree in compact, high efficiency magnetic integration in power electronics for electric vehicle charging applications with the Department of Electrical Engineering, Indian Institute of Technology, Jammu, India.

His research interests include electric vehicle battery chargers, magnetic integration, and dc–dc converters in power electronics.

Arun Kumar Verma (Senior Member, IEEE) received the master’s degree in energy science & engineering and the Ph.D. degree in power electronics from I.I.T. Delhi, New Delhi, India, in 2010 and 2015, respectively.

He is currently working as an Associate Professor with the Indian Institute Of Technology, Jammu, India. During March–July 2024, he was a Visiting Professor with Ontario Tech University, Oshawa, Canada. He was a Postdoctoral Research Fellow (PDF) with the Energy Research Institute (ERI@N), Nanyang Technological University (NTU), Singapore. Before joining NTU Singapore, he worked as a Visiting Graduate Researcher with the Smart Grid Energy Research Center, University of California Los Angeles (UCLA), Los Angeles, CA, USA. His research interests include power electronics, bidirectional power flow, converters for renewable energy and EVs, EV chargers, and AI/ML application to EV.

Dr. Verma was the recipient of the prestigious BASE Fellowship for advanced solar energy research and the prestigious POSOCO Power System Research Award.